The construction and application of a fully flexible computer simulation model for lithium oxide

2004 J. Phys.: Condens. Matter 16 S2795

(http://iopscience.iop.org/0953-8984/16/27/014)

INSTITUTE OF PHYSICS PUBLISHING JOURNAL OF PHYSICS: CONDENSED MATTER

J. Phys.: Condens. Matter **16** (2004) S2795–S2810 PII: S0953-8984(04)72535-7

The construction and application of a fully flexible computer simulation model for lithium oxide

Mark Wilson[1], **Sandro Jahn**[2] **and Paul A Madden**[2]

[1] Department of Chemistry, University College London, 20 Gordon Street, London WC1H 0AJ, UK
[2] Physical and Theoretical Chemistry Laboratory, Oxford University, South Parks Road, Oxford OX1 3QZ, UK

Received 14 November 2003
Published 25 June 2004
Online at stacks.iop.org/JPhysCM/16/S2795
doi:10.1088/0953-8984/16/27/014

Abstract

An aspherical ion model (AIM) is constructed for lithium oxide, Li_2O. The model incorporates both many-body polarization and short-range ion distortion effects. A procedure for extracting the required model parameters by fitting to results from a series of electronic structure calculations is described. The model is tested with respect to both static and dynamic properties. The experimentally observed Cauchy violation in the elastic constants and phonon frequencies are well reproduced as is the onset temperature for superionic behaviour in the Li^+ sublattice. The system is shown to display a peak in the heat capacity as a function of temperature. The correlated and uncorrelated ion dynamics are studied and the origin of the respective solid- and liquid-state Haven ratios is rationalized.

(Some figures in this article are in colour only in the electronic version)

1. Introduction

The atomistic computer modelling of ionic oxide ceramics has a long history. Oxides represent a particularly difficult class of materials to accurately represent with relatively simple potential energy functions. The formation of the doubly charged oxide anion, O^{2-}, is stabilized by the presence of the condensed phase environment (the ion can be considered as sitting in a stabilizing potential well [1–3]). This is distinct from, for example, the iso-electronic F^- ion which is stable as a free ion. As a result, the properties of the oxide ion are relatively sensitive to the details of the confining environment and so the use of the simplest ionic models (in which the constituent ions are represented by charged spheres modelled as having rigid charge densities) may become problematic if such models are to be accurate over appreciable regions of phase space. The basic pair potential-based models may be improved upon by the inclusion

of many-body effects such as those present as a result of ion polarization and by the short-range distortion of the ion shape [4]. The advantage of this approach over electronic structure methodologies is that the models retain the computational tractability of those based on simpler energy functions and, as a result, significant length scales and timescales remain accessible. A potential disadvantage, however, is that the number of parameters required to fully describe these effects may become prohibitive and, as a result, difficult to parametrize. A solution to this problem is to fit these parameters to properties derived directly from electronic structure calculations (such as ion forces, multipoles and cell stresses).

In this paper a fully distortable model for a specific oxide, lithium oxide (Li_2O), is parametrized by reference to well-directed electronic structure calculations. This system represents a useful step from previous work which has focused on MgO [5, 6], the group of alkaline-earth oxides in general [7] and Al_2O_3 [8]. Furthermore, Li_2O is a useful example of a superionic material analogous to the alkaline-earth fluorides CaF_2, SrF_2 and BaF_2 [9]. Li_2O forms an anti-fluorite structure in which the Li^+ cations occupy all of the tetrahedral holes in a face-centred cubic anion sublattice. Unlike the fluorides, in which the anion sublattice becomes mobile at a temperature lower than the melting point, it is the Li^+ cation sublattice which becomes mobile. As a result, the effective modelling of Li_2O represents a useful step both in comparison with the modelling of alkaline-earth (and other) fluorides [10, 11] and towards the modelling of more complex oxides, such as $LiMnO_2$ and $LiCoO_2$, which are important battery materials and in which it is the Li^+ ions which are mobile. Pair potential models have been constructed for this system by reference to both Hartree–Fock [12] and density-functional [13] electronic structure calculations as well as from empirical considerations [14–21]. Such potentials, however, cannot reproduce known properties of Li_2O such as the pronounced Cauchy violation [22].

In this paper a fully distortable ionic model will be constructed for lithium oxide. In section 2 the use of electronic structure calculations is described and the fitting procedure required to fit the AIM parameters is discussed. In addition, the basic AIM is described for completeness. In section 3 the model is tested by reference to the static (lattice parameter and elastic constants) and dynamic (thermal expansivity, phonon dispersion curves, melting point, heat capacity and ion dynamics) properties.

2. Potential model

2.1. The aspherical ion model

The aspherical ion model (AIM) has been described in detail recently [23]. Here, we present a summary for completeness. The functional forms for the AIM are chosen by reference to series of well-directed electronic structure calculations [2, 5, 24, 25]. The potential may be considered as constructed from four components: charge–charge, dispersion, overlap repulsion and polarization. The first two components are purely pairwise additive:

$$V^{qq} = \sum_{i \leqslant j} \frac{q_i q_j}{r_{ij}}, \tag{2.1}$$

where q_i is the (formal) charge on ion i. The dispersion interactions include dipole–dipole and dipole–quadrupole terms

$$V^{\text{disp}} = -\sum_{i \leqslant j} [f_6^{ij}(r^{ij}) C_6^{ij} / r^{ij^6} + f_8^{ij}(r^{ij}) C_8^{ij} / r^{ij^8}], \tag{2.2}$$

where C_6^{ij} and C_8^{ij} are the dipole–dipole and dipole–quadrupole dispersion coefficients respectively, and f_n^{ij} are Tang–Toennies dispersion damping functions [26], which describe

short-range corrections to the asymptotic dispersion term.

The overlap repulsion component is given by

$$V^{\mathrm{rep}} = \sum_{i\in \mathrm{O},\, j\in \mathrm{Li}} [A^{-+}\mathrm{e}^{-a^{-+}\rho^{ij}} + B^{-+}\mathrm{e}^{-b^{-+}\rho^{ij}}] + \sum_{i,\,j\in \mathrm{O}} A^{--}\mathrm{e}^{-a^{--}r^{ij}} + \sum_{i\in \mathrm{O}} [D(\mathrm{e}^{\beta\delta\sigma^i} + \mathrm{e}^{-\beta\delta\sigma^i}) + (\mathrm{e}^{\zeta^2|\boldsymbol{\nu}^i|^2} - 1) + (\mathrm{e}^{\eta^2|\boldsymbol{\kappa}^i|^2} - 1)], \tag{2.3}$$

where

$$\rho^{ij} = r^{ij} - \delta\sigma^i - S^{(1)}_\alpha \nu^i_\alpha - S^{(2)}_{\alpha\beta}\kappa^i_{\alpha\beta}, \tag{2.4}$$

and summation of repeated indexes is implied. The variable $\delta\sigma^i$ characterizes the deviation of the radius of oxide anion i from its default value, $\{\nu^i_\alpha\}$ are a set of three variables describing the Cartesian components of a dipolar distortion of the ion, and $\{\kappa^i_{\alpha\beta}\}$ are a set of five independent variables describing the corresponding quadrupolar shape distortions. (In equation (2.3), $|\kappa|^2 = \kappa^2_{xx} + \kappa^2_{yy} + \kappa^2_{zz} + 2(\kappa^2_{xy} + \kappa^2_{xz} + \kappa^2_{yz})$ and $S^{(1)}_\alpha = r^{ij}_\alpha / r^{ij}$ and $S^{(2)}_{\alpha\beta} = 3r^{ij}_\alpha r^{ij}_\beta / r^{ij^2} - \delta_{\alpha\beta}$ are interaction tensors.) The last summations include the self-energy terms, representing the energy required to deform the anion charge density, with β, ζ and η as effective force constants. The extent of each ion's distortion is determined at each molecular dynamics time step by energy minimization.

Due to the small cation size, the cation–cation repulsion is sufficiently modelled by the Coulomb term. The shape deformations are taken as relatively insignificant for the anion–anion repulsions, which are therefore represented by simple Born–Mayer exponentials. It is worth noting, however, that there is no fundamental reason (beyond an increase in the model complexity) for not including such distortion effects for all interactions.

The polarization part of the potential incorporates dipolar and quadrupolar contributions [27],

$$V^{\mathrm{pol}} = \sum_{i,\,j\in \mathrm{O}} \left((q^i\mu^j_\alpha - q^j\mu^i_\alpha)T^{(1)}_\alpha + \left(\frac{q^i\theta^j_{\alpha\beta}}{3} + \frac{\theta^i_{\alpha\beta}q^j}{3} - \mu^i_\alpha\mu^j_\beta\right)T^{(2)}_{\alpha\beta} + \left(\frac{\mu^i_\alpha\theta^j_{\beta\gamma}}{3} + \frac{\theta^i_{\alpha\beta}\mu^j_\gamma}{3}\right)T^{(3)}_{\alpha\beta\gamma} + \frac{\theta^i_{\alpha\beta}\theta^j_{\gamma\delta}}{9}T^{(4)}_{\alpha\beta\gamma\delta}\right) + \sum_{i\in \mathrm{O},\, j\in \mathrm{Li}} \left(q^j\mu^i_\alpha[1 - g_{\mathrm{D}}(r^{ij})]T^{(1)}_\alpha + \frac{\theta^i_{\alpha\beta}q^j}{3}[1 - g_{\mathrm{Q}}(r^{ij})]T^{(2)}_{\alpha\beta}\right) + \sum_{i\in \mathrm{O}} (k^i_1|\vec{\mu}^i|^2 + k^i_2\mu^i_\alpha\theta^i_{\alpha\beta}\mu^i_\beta + k^i_3\theta^i_{\alpha\beta}\theta^i_{\alpha\beta} + k^i_4|\vec{\mu}^i\cdot\vec{\mu}^i|^2), \tag{2.5}$$

where $k^i_1 = \frac{1}{2\alpha^i}$, $k^i_2 = \frac{B^i}{4\alpha^{i^2}C^i}$, $k^i_3 = \frac{1}{6C^i}$, $k^i_4 = \frac{-B^{i^2}}{16\alpha^{i^4}C^i}$, α^i, B^i and C^i the dipole, dipole–dipole–quadrupole and quadrupole polarizabilities of ion i, respectively, and $T_{\alpha\beta\gamma\delta} = \nabla_\alpha\nabla_\beta\nabla_\gamma\nabla_\delta\cdots\frac{1}{r^{ij}}$ are the multipole interaction tensors [28]. The instantaneous values of these moments are obtained by minimization of this expression. The charge–dipole and charge–quadrupole cation–anion asymptotic functions include terms which account for penetration effects at short range by using Tang–Toennies damping functions [26] of the form,

$$g_{\mathrm{D}}(r^{ij}) = c_{\mathrm{D}}\mathrm{e}^{-b_{\mathrm{D}}r^{ij}} \sum_{k=0}^{4} \frac{(b_{\mathrm{D}}r^{ij})^k}{k!}, \tag{2.6}$$

$$g_{\mathrm{Q}}(r^{ij}) = c_{\mathrm{Q}}\mathrm{e}^{-b_{\mathrm{Q}}r^{ij}} \sum_{k=0}^{6} \frac{(b_{\mathrm{Q}}r^{ij})^k}{k!}, \tag{2.7}$$

with D and Q standing for dipolar and quadrupolar parts. While the parameters b_D and b_Q determine the range at which the overlap of the charge densities affects the induced multipoles, the parameters c_D and c_Q determine the strength of the ion response to this effect. The short-range induction corrections in the anion–anion interactions are neglected and the Li ions are assumed not to be polarizable.

The constructed AIM potential contains seventeen additional degrees of freedom in order to describe the state of the electron charge density of the ions. The ground state configuration of the electronic degrees of freedom at each time step is extracted using a conjugate gradients routine [29], starting from their values at the preceding time step.

2.2. Determining the AIM parameters

The AIM potential parameters are derived by reference to *ab initio* DFT calculations performed on atomic configurations for several condensed phases, in which significantly different coordination environments are sampled. The atomic configurations are derived from high temperature MD simulations in the isothermal–isobaric (NpT) [30] ensemble on the fluorite crystal structure and the liquid using an existing effective pair potential [12]. The pair potential used [31] should be good enough to generate representative configurations (as evidenced by its relative success in simulating known properties of Li_2O [12]).

Atomic configurations from each run are selected and the *ab initio* forces, stresses and multipole moments are extracted for each of the ions in them using the plane-wave (periodic boundary condition) DFT CASTEP code [32][3]. The AIM parameters are then optimized such that the forces, stresses and multipole moments calculated with the AIM for the same atomic configurations reproduce the respective *ab initio* values.

2.2.1. Calculating the ab initio forces, stresses and multipoles. For the CASTEP calculations, norm-conserving, non-local ultrasoft pseudopotentials for all the ions have been used, together with a kinetic energy cut-off of 580 eV on a $60 \times 60 \times 60$ FFT grid and the PW91 GGA exchange–correlation functional [33, 34]. Our plane-wave cut-offs are considerably larger than would normally be used in order to ensure a high degree of convergence of the forces with respect to basis set size. A finite basis set correction to the stress tensor [32] was estimated by performing calculations at three different values of the kinetic energy cut-off.

The electronic wavefunctions are the Kohn–Sham orbitals and are delocalized throughout the simulation cell. To allow for the association of orbitals with each ion a localized representation of the electron density distribution is generated via a Wannier transformation [35, 36]. Under the condition of maximal localization [37] a set of Wannier (or Boys) orbitals is obtained which provides a picture of the electron distribution around ions polarized by the interactions with the surrounding environment. A complete theory of electric polarization in crystalline dielectrics has been developed in recent years [38–42], which validates the calculation of the dipole moments of single ions from the centre of charge of the subset of maximally localized Wannier functions (MLWFs) which are localized in their vicinity [43, 44]. In addition, it has been recently shown how ion quadrupole moments may be extracted in analogous fashion [23].

The MLWFs [37] are determined by unitary transformations of the Kohn–Sham eigenvectors

$$w_n(\mathbf{r}) = \sum_{m=1}^{J} \mathrm{U}_{mn} |\phi_m\rangle, \tag{2.8}$$

[3] We used the code CASTEP 3.9 academic version, licensed under the UKCP-MSI Agreement, 1999.

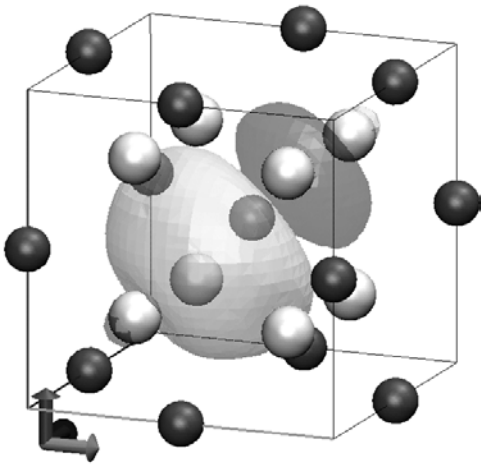

Figure 1. A very low density isosurface of one of the O^{2-}-centred MLWFs for Li_2O in the anti-fluorite structure, with the central O^{2-} ion diagonally displaced from its equilibrium site. White and dark balls represent the Li and O ions, respectively.

where the sum runs over all the Kohn–Sham states ϕ_i, and the unitary matrix $\mathbf{U}$ is determined by iterative minimization of the Wannier function spread [37]

$$\Omega = \sum_{n=1}^{J} (\langle r^2 \rangle_n - \langle \mathbf{r} \rangle_n^2). \tag{2.9}$$

Figure 1 shows a low density isosurface of a single MLWF centred close to an O^{2-} ion. The charge density is well localized within the range of nearest neighbours, as expected for an ionic system. With the 1s orbital pseudized, four MLWFs are found in the vicinity of each oxygen atom. There is also one MLWF attached to each Li atom. The latter are much more localized with a Wannier spread being about a factor of two smaller than the respective MLWFs of the anions. Their isosurfaces have a spherical shape and resemble the Li 1s orbitals.

The Wannier function centre (WFC) positions are computed according to [45, 46]

$$(r_\alpha)_n = -\sum_{\beta=1}^{3} \frac{M^{-1}_{\alpha\beta}}{b_\beta} \operatorname{Im} \ln[\mathbf{U}^\dagger \mathbf{K}^{(\beta)} \mathbf{U}]_{\mathbf{nn}}, \qquad \alpha = 1, 2, 3, \tag{2.10}$$

with $r_1 = x$, $r_2 = y$, $r_3 = z$. $M_{\alpha\beta} = (\mathbf{b}_\alpha \cdot \hat{\mathbf{u}}_\beta) b_\alpha^{-1}$ is the normalized projection of the αth reciprocal lattice vector on the βth Cartesian unit vector, and

$$K^{(\beta)}_{ij} = \langle \phi_i | \mathrm{e}^{-\mathrm{i}\mathbf{b}_\beta \cdot \mathbf{r}} | \phi_j \rangle. \tag{2.11}$$

The components of the electronic contribution to the total dipole moment $\mathbf{p}$ can be estimated from the WFC positions,

$$\mathbf{p} = -2 \sum_{n=1}^{J} \mathbf{r}_n, \tag{2.12}$$

where the sum runs over the total number of electronic states. Since the MLWFs are localized, partial dipole moments may be associated with subsets of states grouped around a single centre allowing for separation of charge density into the contributions from single ions. The ionic partial dipole moments for each ion I are defined by,

$$\mu^{\mathrm{I}}_\alpha = -2 \sum_{n \epsilon \mathrm{I}} r_{n,\alpha} + Z_{\mathrm{I}} R_{\mathrm{I},\alpha}, \tag{2.13}$$

where the sum runs over those MLWFs which are close to ion I, and $Z_{\rm I}$ is the charge of the pseudopotential core in the position $\mathbf{R}_{\rm I}$.

The components of the quadrupole on ion I are evaluated from the real-space integral of the charge densities of the MLWFs

$$\theta^{\rm I}_{\alpha\beta} = -2\sum_{n\epsilon {\rm I}} \int_{V^{\rm I}_{\rm cut}} \mathbf{dr}\, |w_n(\mathbf{r})|^2 (1/2)(3r^{\rm I}_\alpha r^{\rm I}_\beta - (r^{\rm I})^2\delta_{\alpha\beta}). \tag{2.14}$$

Here the integral runs over the space within a sphere of radius $r_{\rm cut}$ around I, and $\mathbf{r}^{\rm I}$ is the distance from $\mathbf{r}$ to the nucleus of I calculated with a minimum image convention: the factor of -2 accounts for the two electrons in each MLWF and the electronic charge.

2.2.2. Fitting procedure. The polarization terms in the AIM are optimized first by varying the set $\{\chi_P\}$ of relevant parameters in order to minimize the objective function

$$A_P(\{\chi_P\}) = \frac{1}{2N_{\rm O}} \sum_{i\in {\rm O},A} \left(\frac{|\vec{\mu}^A_i(\{\chi_P\}) - \vec{\mu}^{A,ai}_i|^2}{|\vec{\mu}^{A,ai}_i|^2} + \frac{|\vec{\theta}^A_i(\{\chi_P\}) - \vec{\theta}^{A,ai}_i|^2}{|\vec{\theta}^{A,ai}_i|^2} \right) \tag{2.15}$$

with the index i running over the anions of one configuration and $N_{\rm O}$ being the total number of anions of all configurations. The different sets of configurations on which the multipoles have been calculated are labelled by the index A. $\vec{\mu}_i$ comprises the three components of the induced dipole on atom i, μ_x, μ_y and μ_z, while $\vec{\theta}_i$ is the vector of the five independent components of the respective tensor of the quadrupole moment, $\theta_{i,\alpha\beta}$. $\vec{\mu}^A_i(\{\chi_P\})$ and $\vec{\theta}^A_i(\{\chi_P\})$ refer to the multipoles calculated from the model (for ion i) in configuration A with the parameter set $\{\chi_P\}$, $\vec{\mu}^{A,ai}_i$ and $\vec{\theta}^{A,ai}_i$ are the corresponding *ab initio* values.

Standard simplex and gradient minimization algorithms [29] are used to minimize the objective function (2.15) over the full set of all dipoles and quadrupoles for every ion in all configurations simultaneously. At each step of the fitting procedure the polarization energy $V_{\rm pol}$ (2.5) is minimized to obtain the 'adiabatic' dipoles and quadrupoles. All the parameters in the polarization potential are allowed to vary (the polarizabilities α, B and C and the damping parameters b and c).

In the second step of the fitting procedure all parameters entering the short-range repulsion part of the potential (equation (2.3)) are optimized. Now the polarization parameters $\{\chi_P\}$ remain fixed and the set of short-range potential parameters $\{\chi_{\rm sr}\}$ is varied to minimize the objective function

$$A_F(\{\chi_{\rm sr}\}) = \frac{1}{2N_{\rm tot}} \sum_{i,A} \frac{|\vec{F}^A_i(\{\chi_{\rm sr}\}) - \vec{F}^{A,ai}_i|^2}{|\vec{F}^{A,ai}_i|^2} + \frac{1}{2N_A} \sum_A \frac{|\vec{S}^A(\{\chi_{\rm sr}\}) - \vec{S}^{A,ai}|^2}{|\vec{S}^{A,ai}|^2}, \tag{2.16}$$

to match the AIM forces and stress tensors to the *ab initio* results. Now the index i runs over all ions of configuration A. $\vec{F}^{A,ai}_i$ and $\vec{S}^{A,ai}$ refer to the force on ion i and a vector containing the stress tensor elements extracted from the *ab initio* calculation of configuration A, and $\vec{F}^A_i(\{\chi\})$ and $\vec{S}^A(\{\chi\})$ to those calculated from the AIM with parameters $\{\chi_{\rm sr}\}$ at exactly the same ionic configuration. N_A is the number of atomic configurations and $N_{\rm tot}$ the total number of ions included in the force fit. The dispersion interactions are included in the evaluation of the objective function A_F but the dipole–dipole (C^{ij}_6) and dipole–quadrupole (C^{ij}_8) dispersion coefficients are fixed to the values given in [24, 47] (and so are very close to what is obtained from the dipole polarizabilities of the ions by applying Slater–Kirkwood and Starkschall–Gordon formulae, respectively [48]). Tang–Toennies dispersion damping parameter (for the functions f_6 and f_8) are fixed at values previously derived to model MgO. The quality of the fit of the objective function is found to be insensitive to allowing these terms to vary.

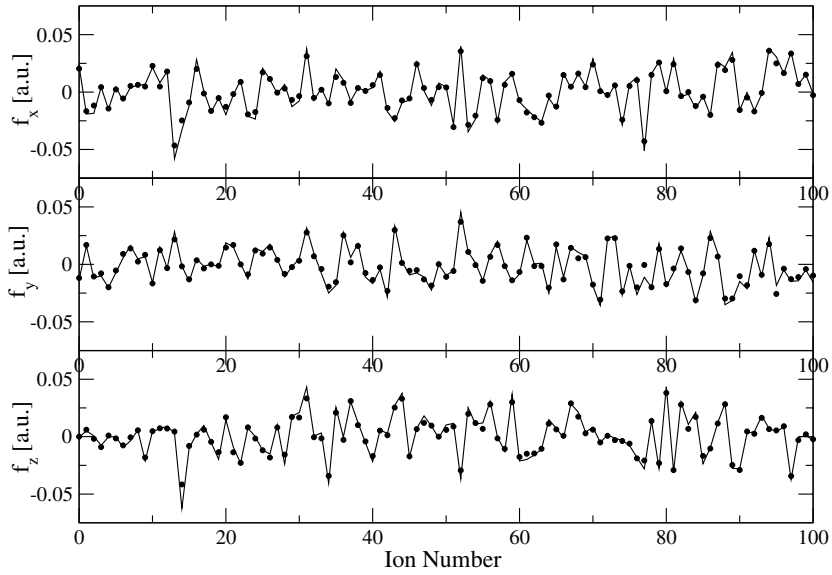

Figure 2. The quality of the force fit demonstrated for a set of 100 representative ions. The solid curves connect results obtained from the AIM with the final set of parameters, the points indicate the respective *ab initio* forces. The first 50 ions are Li^+ ions taken from a liquid configuration of Li_2O. The other 50 ions represent O^{2-} ions from a high pressure solid configuration.

For the potential optimization of Li_2O we used four configurations, each of them containing 324 ions. These configurations were extracted from simulations performed with an existing effective pair potential and were taken from runs on the low and high temperature anti-fluorite crystal (below and above the superionic transition temperature respectively) and the liquid (from which two independent configurations were extracted). The use of relatively large cells is to avoid the difficulties associated with truncation of the short-range exponentials and the consequential truncation correction to the stress tensor.

Uniformly good fits were obtained across the range of configurations sampled. The quality of the fits is illustrated in figure 2 for the three force components of 100 representative ions taken from a solid and a liquid configuration. The solid lines connect the predicted forces on the ions predicted from the AIM, whereas the dots indicate the corresponding *ab initio* forces. The quality of the fit to the stress tensors and the dipoles is equally good (objective function around or smaller than 0.1), although the magnitudes of the quadrupole components obtained with the AIM are found to be systematically too small compared to the *ab initio* values.

Tables 1 and 2 list the fitted AIM parameters required to complete the equations listed in the previous sections. An important outcome of the fitting procedure is that the derived parameters should retain their physical meaning. For example, in the present work the dipole polarizability, α, should be close to that derived from the experimental refractive index. Such a procedure gives a value of $\alpha_{O^{2-}} = 14.17$ au [49] compared with the fitted values of 13.76 au. In addition, the short-range damping parameters sets, $\{b_D, c_D, b_Q, c_Q\}$, can be compared with those derived directly for other systems by performing *ab initio* electronic structure calculations in which multipoles are generated using specifically distorted crystalline environments [25]. The values for this parameter set listed in the tables are fully consistent with those considered previously [25].

Table 1. Parameters in the repulsive and polarization parts of the potential. All values are in atomic units.

	A	a	B	b	Self-CIM	Self-AIM	b^{pol}	c^{pol}
$-+$	30.91	1.748	8763	4.573	$D = 0.381$	$\zeta = 1.297$	$b_{\mathrm{D}} = 1.701$	$c_{\mathrm{D}} = 1.431$
$--$	21 657	2.9684	—	—	$\beta = 0.740$	$\eta = 2.723$	$b_{\mathrm{Q}} = 1.657$	$c_{\mathrm{Q}} = 1.227$

Table 2. Polarizabilities, dispersion coefficients (dipole–dipole and dipole–quadrupole) and dispersion damping parameters. All values are in atomic units.

	α	B	C		C_6	C_8	b^{disp}
O^{2-}	13.76	−68.8	25.24	$-+$	2.2	25.3	2.21
—	—	—	—	$--$	110.0	1800	1.44
				$++$	0.22	0.86	—

Table 3. Static (0 K) lattice constants (a_0), bulk moduli (B) and elastic constants ($C_{\alpha\beta}$).

Property	AIM	Expt[a] [22]	DFT [13]	HF [52]	HF [53]
a_0 (Å)	4.607	4.574	4.533	4.573	4.570
B (GPa)	80	88	89	92.6	94.6
C_{11} (GPa)	202	217	238	—	—
C_{12} (GPa)	19	24	16	—	—
C_{44} (GPa)	59	68	66	—	—
Δ (GPa)	−40	−44	−50	—	—
A	0.64	0.70	0.59	—	—

[a] Extrapolation to 0 K. Δ ($\equiv C_{12} - C_{44}$) is a measure of the magnitude of the Cauchy violation. A is the elastic anisotropy factor, $A = 2C_{44}/(C_{11} - C_{12})$.

3. Results

3.1. Static properties

Table 3 lists the static (0 K) properties calculated using the fitted AIM. The 0 K lattice parameter, extracted from the calculated static energy/volume curve, is in excellent agreement with experiment [51] being ∼0.7% greater. Furthermore, the experimental value is derived from the temperature-dependent data at temperatures starting from 293 K and, as a result, the method by which the lattice parameter is extrapolated to 0 K is open to interpretation.

Table 3 also lists the calculated bulk modulus, B, and elastic constants, $C_{\alpha\beta}$, compared with those determined experimentally [22] and those calculated using electronic structure methodologies [13, 52, 53]. The bulk modulus is calculated by fitting a fifth order polynomial to the energy/volume curves and using the relationship, $B = V\frac{\mathrm{d}^2U}{\mathrm{d}V^2}$. The model value is in excellent agreement with experiment and the values derived from the electronic structure calculations. C_{11} and C_{12} are calculated from the bulk modulus and the relation $B \equiv \frac{1}{3}(C_{11} + 2C_{12})$ and the shear modulus ($C_s = \frac{1}{2}(C_{11} - C_{12})$). In order to calculate the shear modulus the strain matrix

$$\epsilon = \begin{pmatrix} \frac{2\delta}{3} & 0 & 0 \\ 0 & \frac{-\delta}{3} & 0 \\ 0 & 0 & \frac{-\delta}{3} \end{pmatrix}, \tag{3.1}$$

is applied with δ ranging from −0.006 to +0.006 au (within the harmonic range). The elastic

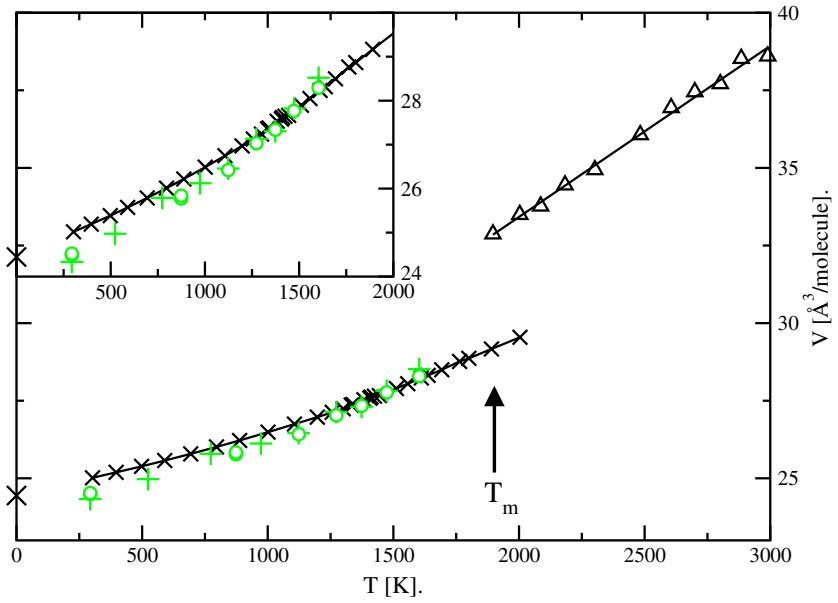

Figure 3. Calculated equilibrium volumes as a function of temperature for the Li_2O AIM in the anti-fluorite crystal (×) and the liquid states (△). The approximate melting point, as determined in this work, is indicated by the arrow. The experimental crystal data from [22, 56] (+) and [51] (○) are also shown. The inset shows a magnified section of the solid crystal curve in order to highlight the change in gradient (at ∼1450 K) associated with the change in volume across the superionic transition.

constant C_{44} is calculated using the following strain matrix with the same δ-values,

$$\epsilon_2 = \begin{pmatrix} 0 & \frac{\delta}{2} & \frac{\delta}{2} \\ \frac{\delta}{2} & 0 & \frac{\delta}{2} \\ \frac{\delta}{2} & \frac{\delta}{2} & 0 \end{pmatrix}. \tag{3.2}$$

As for the bulk modulus, the calculated values for the elastic constants are in excellent agreement with both experimental and density-functional values. Again, the experimentally determined elastic constants are susceptible to error as they are extracted by extrapolating finite-temperature data to 0 K. Significantly, the magnitude and sign of the Cauchy violation ($\Delta = C_{12} - C_{44}$) are both in excellent agreement with experiment. The Cauchy violation is the direct result of the presence of non-central forces in the model (in a model with only pairwise interactions the relation $C_{12} = C_{44}$ must hold). As a result, the Cauchy violation is a direct measure of the magnitude of the many-body short-range distortions of the oxide anions in the present model.

3.2. 'Simple' dynamic properties

Figure 3 shows the equilibrium system volume as a function of temperature for both the crystalline (anti-fluorite structure) solid and the liquid states. Each volume is determined by performing constant temperature and pressure molecular dynamics, applied using Nosé–Hoover thermostats and barostats respectively [54, 30]. The experimental crystal volume is shown for comparison [51]. The calculated thermal expansivity of 2.92×10^{-5} K^{-1} compares with experimental values of 3.36×10^{-5} K^{-1} [22] and 3.29×10^{-5} K^{-1} [55]. This value

has been calculated over the temperature range 300–1150 K, below the superionic transition temperature and consistent with the experimental analysis. As highlighted in the inset, the rate of change of the volume with temperature undergoes a significant change at ∼1450 K consistent with the change seen in the experimental data (see figure 4 of [22]). We anticipate that this change in gradient corresponds to the onset of superionic behaviour. The calculated value for the liquid is 8.0×10^{-5} K^{-1} in the temperature range 2000–3000 K.

The phonons are calculated from the simulations using the following equations for the longitudinal and transverse currents of the charge, mass and a third variable which picks out the relative motion of Li^+ ions. Fourier transformation of these current correlation functions produces peaks which give the phonon frequencies at a particular **k**-vector. The longitudinal correlation function, C^{L}_{XX}, for the variable X^j ($=Q^j$, the charge on ion j, for example) is given by

$$C^{\mathrm{L}}_{XX}(\mathbf{k},t) = \left\langle \left(\sum_{j=1}^{N} -X^j(t) i\mathbf{k}\cdot\mathbf{v}^j(t) \mathrm{e}^{-\mathrm{i}\mathbf{k}\cdot\mathbf{r}^j(t)} \right) \left(\sum_{l=1}^{N} X^l(t) \mathrm{i}\mathbf{k}\cdot\mathbf{v}^l(t) \mathrm{e}^{-\mathrm{i}\mathbf{k}\cdot\mathbf{r}^l(t)} \right) \right\rangle, \tag{3.3}$$

whilst the transverse correlation function is given by:

$$C^{\mathrm{T}}_{XX}(\mathbf{k},t) = \left\langle \left(\sum_{j=1}^{N} -X^j(t) \mathrm{i}\mathbf{k}\wedge\mathbf{v}^j(t) \mathrm{e}^{-\mathrm{i}\mathbf{k}\cdot\mathbf{r}^j(t)} \right) \left(\sum_{l=1}^{N} X^l(t) \mathrm{i}\mathbf{k}\wedge\mathbf{v}^l(t) \mathrm{e}^{-\mathrm{i}\mathbf{k}\cdot\mathbf{r}^l(t)} \right) \right\rangle. \tag{3.4}$$

The frequencies at **k**-vectors along three high symmetry directions, $\{\xi,0,0\}$, $\{\xi,\xi,0\}$ and $\{\xi,\xi,\xi\}$, are calculated in order to allow for direct comparison with the experimental phonon dispersion curves [56]. With $X^j = Q^j$, the optic mode peak dominates the spectrum, and for $X^j = M^j$ (ion mass) the acoustic branch is dominant. In order to obtain the second 'optic' branch, X^j is set equal to unity for ions on one of the two Li^+ fcc sublattices, which together make up the simple cubic lattice of Li^+ in the anti-fluorite structure, and to minus one for the other sublattice. Three simulation cells, corresponding to $3\times3\times3$, $4\times4\times4$ and $5\times5\times5$ units cells (324, 768 and 1500 ions respectively) are used in order to give an appreciable sampling of the Brillouin zone along the three high symmetry directions. The choice of these three cells allows for the ξ sets $(\frac{1}{3},\frac{2}{3},1)$, $(\frac{1}{4},\frac{1}{2},\frac{3}{4},1)$ and $(\frac{1}{5},\frac{2}{5},\frac{3}{5},\frac{4}{5},1)$ to be sampled.

Figure 4 shows the calculated phonon dispersion curves along the three high symmetry directions considered. The figure also shows the curves generated using a shell model fitted directly to the experimental data [56, 57]. The calculated dispersion curves are, in general, in excellent agreement with experiment especially considering the massive contributions to the phonon mode frequencies of the inclusion of the anion distortions [5, 24]. The acoustic mode frequencies are near perfect as the Γ-point is approached, reflecting the accuracy of the elastic constants discussed above. Regarding the optic dispersion curves, the TO2 mode frequencies are generally lower than those observed experimentally. Considering the nature of this mode (see, for example, the discussion of these mode frequencies with respect to the fluorite-structured PbF_2 in [11]) this may indicate that the oxide anion is slightly too dipolar distortable. The LO1 mode frequencies are, however, in excellent agreement with experiment indicating that the quadrupolar distortions of the oxide ion are well behaved [11]. Furthermore, the relatively 'flat' shape of this curve along X $\longrightarrow$ Γ in the [ξ00] direction is reproduced.

3.3. Melting point

The zero pressure melting point can be estimated by direct simulation of the liquid/solid interface [58]. Here, the interfaces are constructed by combining two separate simulation cells containing fluorite crystal and liquid configurations respectively, corresponding to equilibrated configurations generated at state points near the estimated coexistence temperature. Cells

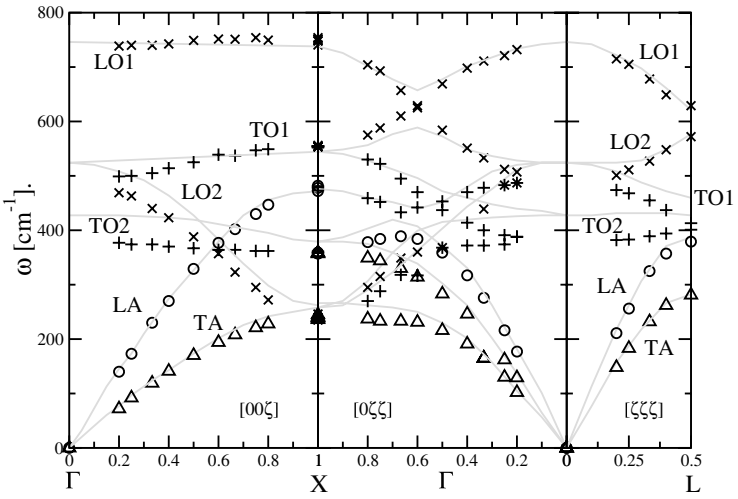

Figure 4. Phonon dispersion curves for the Li_2O AIM at 298 K calculated along the three high symmetry directions indicated. The light grey lines represent the mode frequencies calculated using a shell model fitted to the experimental data [56, 57]. Key to the modes: ×—longitudinal optical, +—transverse optical, ○—longitudinal acoustic, △—transverse acoustic.

containing the equilibrated crystal and liquid configurations, are combined to give a tetragonal simulation cell elongated along a single axis with the liquid/solid interface set up so as to be perpendicular to the crystal [100] direction. The cell is periodically repeated in three dimensions giving an infinite series of liquid/solid slabs containing two interfaces per simulation cell. Simulations are performed in the NpT ensemble using the initial ion velocities carried over from the separate crystal and liquid simulations. The ions in the initial configurations, in particular in the interfacial region, are in poor equilibrium. The use of the Nosé–Hoover thermostats acts to control any rise in temperature associated with the relaxations in these regions and hence prevents uncontrolled melting or recrystallization at the interface. Once the system has been properly re-equilibrated the temperature is systematically varied until the liquid and crystal are in equilibrium [59] as monitored by reference to the time evolution of the system energy.

Figure 5 shows a molecular graphics 'snapshot' of the simulation cell containing the liquid/solid interface. The system contains 216 molecules originally in the crystal and a further 216 molecules originally in the liquid cell. The motion of the interface may also usefully be monitored by constructing time-dependent ion density profiles perpendicular to the interface (as shown in the figure). The present AIM gives a melting point of ∼1900 K compared with the experimental value of 1705 K [50]. The calculation uses an ideal (defect free) crystal slab and so, since the real system melting point would be expected to be heavily influenced by the presence of defects, our value represents an upper limit to the model transition temperature.

3.4. Heat capacities

The heat capacity of these systems is known to be a useful indicator of the onset of superionic behaviour. Type-II superionic materials, such as the alkaline-earth fluorides, exhibit a so-called Bredig transition [60] which is characterized by a (λ-) peak present in the heat capacity. The heat capacity is calculated from the internal energies of the crystals as a function of temperature and, since each system has been pre-equilibrated to zero pressure, we are measuring C_p.

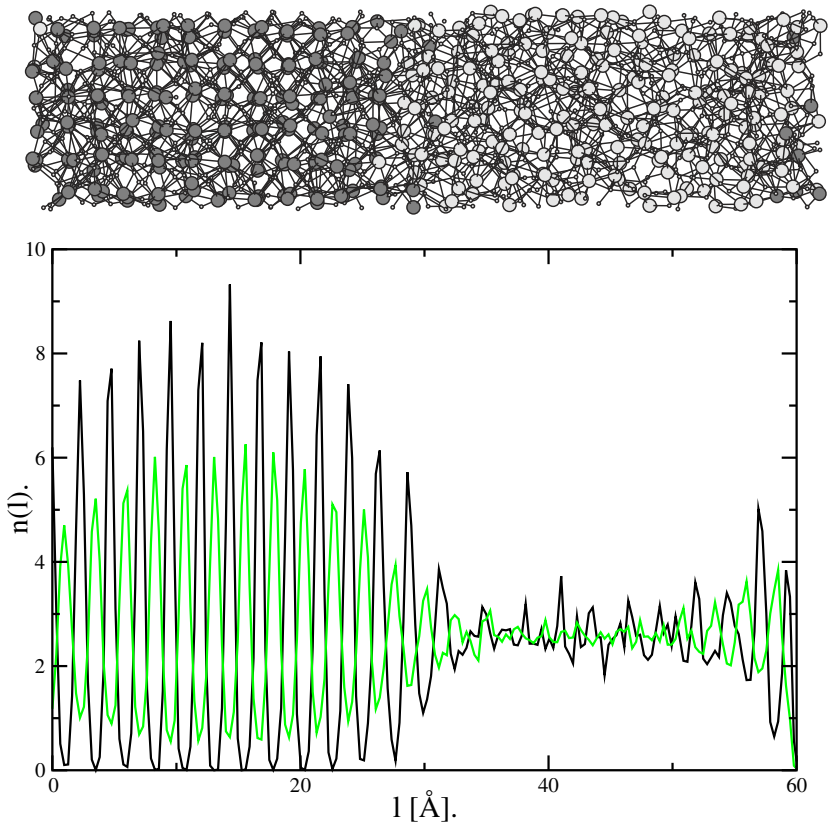

Figure 5. A molecular graphics 'snapshot' of the solid/liquid interface system at the estimated melting point of 1900 K. The light circles represent those anions originally in the liquid configuration, and the darker circles those originally in the crystal. The small circles represent the cations. The lower panel shows a density profile (projected as for the snapshot) at this temperature calculated over ∼5 ps of molecular dynamics. The dark and light lines represent the cation and anion distribution respectively.

Figure 6 shows the calculated heat capacity for the present system compared with that recently generated for CaF_2 [10]. The peak in C_p occurs at ∼1450 K compared with the experimentally estimated temperature marking the onset of superionic behaviour at 1350 K (estimated from the change in gradient of the elastic constants with temperature) [51]. The peak rises from a level of $\sim 9R$ prior to the superionic transition (equivalent to the Debye limit for a harmonic solid) to a height of $\sim 14.5R$ (∼120.6 J mol^{-1} K^{-1}). The entropy associated with the transition may be estimated using the area under this curve,

$$\Delta S = \int_{\text{peak}} \frac{C_p}{T}\,\mathrm{d}T. \tag{3.5}$$

A simple integration of this function, removing a background of $9R$, results in $\Delta S = 14.1$ J mol^{-1} K^{-1}. However, if one uses the experimental values for Li_2O (available for temperatures less than 1125 K—see [22] and references therein) coupled with a linear extrapolation (as discussed in [22] and shown in figure 6) a much smaller value of $\Delta S = 5.8$ J mol^{-1} K^{-1} results. These values are consistent with those calculated for the fluorite systems [10, 11]. However, the variation in values depending on the integration procedure prevents a useful detailed comparison.

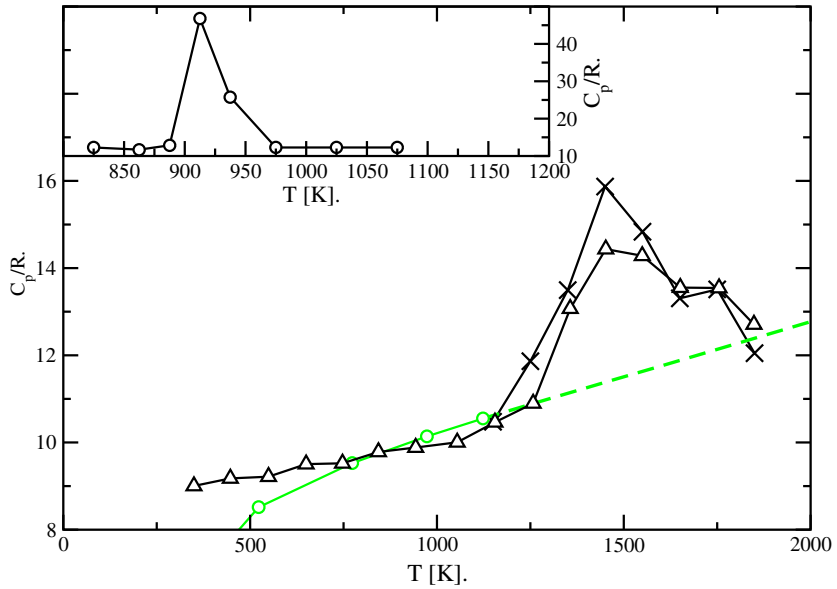

Figure 6. The heat capacity calculated for the Li_2O AIM (△) compared with that calculated for CaF_2 (×) [10] and PbF_2 (inset) [11]. The light circles represent the experimental heat capacities and the light dashed line the extrapolation of these data to temperatures greater than 1125 K (as shown in [22]).

3.5. Conductivity and diffusion

The ionic conductivity can be formally expressed in terms of the charge current correlation function [61]

$$\lambda^K = \frac{\beta e^2}{V} \int_0^\infty J(t)\,\mathrm{d}t, \tag{3.6}$$

where $\beta = 1/kT$, e is the electronic charge and J is a charge current correlation function. We have found it more convenient to examine the long-time limit of an equivalent expression in terms of the mean squared displacement of the charge density [11]:

$$\lambda^K = \frac{\beta e^2}{V} \lim_{t\to\infty} (6t)^{-1} \langle |Q_+ \mathbf{\Delta}_+(t) + Q_- \mathbf{\Delta}_-(t)|^2 \rangle, \tag{3.7}$$

where $\mathbf{\Delta}_\alpha(t)$ is the *net* displacement of all the ions of species α in time t

$$\mathbf{\Delta}_\alpha(t) = \sum_{i\epsilon\alpha} \delta\mathbf{r}_i(t), \tag{3.8}$$

where $\delta\mathbf{r}_i(t)$ is the displacement of ion i in time t. A plot of the mean squared charge displacement appearing in the angle brackets *versus* time, becomes linear after the short-time correlations have died out, and the conductivity can be calculated from this slope.

If all the correlations between ionic displacements are ignored ($\langle \delta\mathbf{r}_i(t)\delta\mathbf{r}_j(t)\rangle = 0$ for $i \neq j$) we obtain the Nernst–Einstein approximation to the conductivity in an equivalent form:

$$\lambda^{\mathrm{NE}} = \beta e^2 \lim_{t\to\infty} (6t)^{-1} [Q_+^2 \rho_+ \langle |\boldsymbol{\delta}_+(t)|^2 \rangle + Q_-^2 \rho_- \langle |\boldsymbol{\delta}_-(t)|^2 \rangle], \tag{3.9}$$

where $\boldsymbol{\delta}_\alpha(t)$ is the displacement of a *single* ion of species α. From the usual relationship between the mean squared displacement and diffusion coefficient this is just

$$\lambda^{\mathrm{NE}} = \beta e^2 (\rho_+ Q_+^2 D_+ + \rho_- Q_-^2 D_-), \tag{3.10}$$

where ρ_α and D_α are the number density and diffusion coefficient of species α.

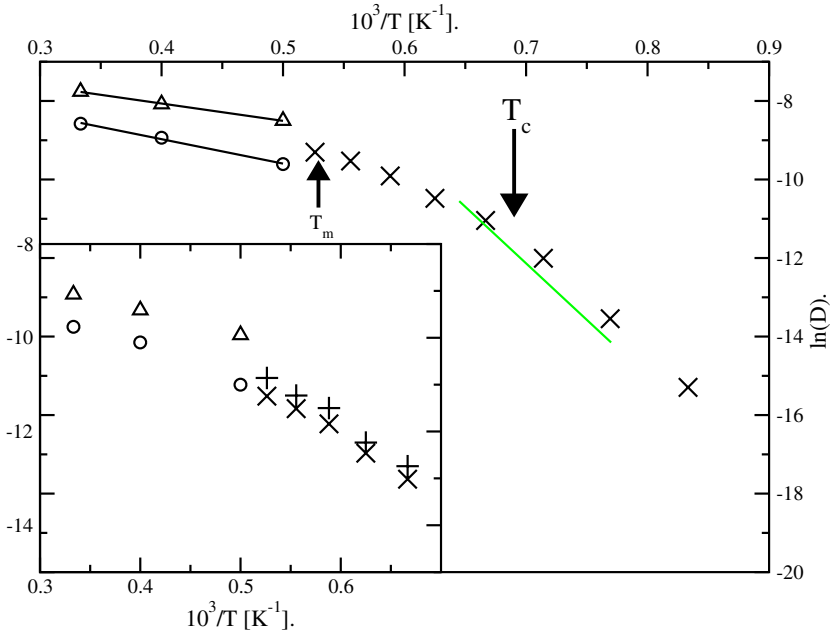

Figure 7. Diffusivity data (main panel) plotted in Arrhenius form for the Li^+ cation in the crystal (×) and the Li^+ (△) and O^{2-} (○) ions in the liquid. The light line shows the diffusion coefficients extracted from experimental conductivity data [62]. The inset shows the time correlation function gradients from equations (3.7) and (3.10) required to calculate the Nernst–Einstein (×—crystal, △—liquid) and collective (+—crystal, ○—liquid) conductivities respectively.

Figure 7 shows the diffusivity data (plotted in Arrhenius form) for the mobile ions in both the liquid and superionic crystal states. The liquid and crystalline diffusion coefficients are calculated from simulations of total length 130 and 150 ps respectively at each temperature. The inset of the figure shows a plot of the gradients required to calculate λ^{NE} and λ^{K} (in equations (3.10) and (3.7) respectively) plotted in analogous form. The Nernst–Einstein calculated values show a characteristic jump in gradient (and hence in calculated conductivity) at the system melting point, simply resulting from the greater ion mobility as a function of temperature and the melting of the anion sublattice. The inclusion of the collective effects, however, leads to significantly different behaviour with the gradient of the time correlation function (and hence the conductivity) falling on system melting. This behaviour can be associated with the difference in collective effects present in the solid and liquid states. In the former, only the Li^+ cations are mobile and so the collective motion appears to increase the motion of the positive charge with respect to the single-ion value (Haven ratio greater than one). Conversely, in the liquid state both ion species are in motion with the generally observed result that the anion and cation charge densities tend to move in a highly correlated fashion. As a result, the overall collective conductivity appears smaller than would be expected from considering the single-ion motion (Haven ratio less than one).

4. Conclusions

In this paper a fully flexible aspherical ion model has been derived for lithium oxide by fitting a range of ion and cell properties to a series of electronic structure calculations. The AIM

has been shown to reproduce a range of both static and dynamic properties, in particular, reproducing the phonon dispersion curves and the pronounced Cauchy violation in the elastic constants. The system undergoes a transition to a superionic state at ∼1450 K (as measured by the peak in the heat capacity) and melts at ∼1900 K. The accuracy and efficiency of the model parametrization demonstrates the effectiveness of both the model and the parametrization methodology.

Acknowledgments

MW thanks the Royal Society for a Research Fellowship. The work was supported by EPSRC grants GR/S06233/01 and GR/R57584/01.

References

[1] Mahan G D and Subbaswamy K R 1990 *Local Density Theory of Polarizability* (London: Plenum)
[2] Fowler P W and Madden P A 1985 *Phys. Rev.* B **31** 5443
[3] Pyper N C 1991 *Adv. Solid State Chem.* **2** 223
[4] Madden P A and Wilson M 1996 *Chem. Soc. Rev.* **25** 339
[5] Rowley A, Ĭemmer P, Wilson M and Madden P A 1998 *J. Chem. Phys.* **108** 10209
[6] Aguado A, Bernasconi L and Madden P A 2002 *Chem. Phys. Lett.* **356** 437
[7] Aguado A, Bernasconi L and Madden P A 2003 *J. Chem. Phys.* **118** 5704
Aguado A and Madden P A 2003 *J. Chem. Phys.* **118** 5718
[8] Jahn S, Madden P A and Wilson M 2004 *Phys. Rev.* B **69** 020106(R)
[9] Chandra S 1981 *Superionic Solids. Principles and Applications* (Amsterdam: North-Holland)
[10] Dent A, Madden P A and Wilson M 2004 *Solid State Ion.* at press
[11] Castiglione M J and Madden P A 2001 *J. Phys.: Condens. Matter* **13** 9963
[12] Fracchia R M, Barrera G D, Allan N L, Barron T H K and Mackrodt W C 1998 *J. Phys. Chem. Solids* **59** 435
[13] García Rodeja J, Meyer M and Hayoun M 2001 *Modelling Simul. Mater. Sci. Eng.* **9** 81
[14] Jacobs P W M and Vernon M L 1993 *J. Chem. Soc., Farad. Trans.* **86** 1233
[15] De Vita M L, Manassidis Y, Lin J S and Gillan M J 1992 *Europhys. Lett.* **19** 605
[16] Gavartin J L, Catlow C R A, Shluger A L, Varaksin A N and Kolmogorov Yu N 1992 *Modelling Simul. Mater. Sci.* **1** 29
Gavartin J L, Shluger A L and Catlow C R A 1993 *J. Phys.: Condens. Matter* **5** 7397
[17] Bush T S, Gale J D, Catlow C R A and Battle P D 1994 *J. Mater. Chem.* **4** 831
[18] Zhoa L X, Hardy J R and Cao H Z 1996 *Solid State Commun.* **99** 637
[19] Catlow C R A, Norgett M J and Ross T A 1977 *J. Phys. C: Solid State Phys.* **10** 1627
[20] Catlow C R A 1989 *Superionic Solids and Solid Electrolytes* (New York: Academic)
[21] Chadwick A V, Flack K W, Strange J H and Harding J H 1988 *Solid State Ion.* **28–30** 185
[22] Hull S, Farley T W D, Hayes W and Hutchings M T 1988 *J. Nucl. Mater.* **160** 125
[23] Aguado A, Bernasconi L, Jahn S and Madden P A 2003 *Faraday Discuss.* **124** 171
[24] Wilson M, Madden P A, Pyper N C and Harding J H 1996 *J. Chem. Phys.* **104** 8068
[25] Ĭemmer P, Fowler P W, Wilson M and Madden P A 1999 *J. Chem. Phys.* **111** 2038
Domene C, Fowler P W, Madden P A, Wilson M and Wheatley R J 2001 *Chem. Phys. Lett.* **333** 403
Domene C, Fowler P W, Madden P A, Xu J, Wheatley R J and Wilson M 2001 *J. Phys. Chem.* A **105** 4136
[26] Tang K T and Toennies J P 1984 *J. Chem. Phys.* **80** 3726
[27] Wilson M, Madden P A and Costa Cabral B J 1996 *J. Phys. Chem.* **100** 1227
[28] Stone A J 1996 *Theory of Intermolecular Forces* (Oxford: Oxford University Press)
[29] Press W H, Flannery B P, Teukolski S A and Vetterling W T 1992 *Numerical Recipes* (Cambridge: Cambridge University Press)
[30] Martyna G J, Tobias D J and Klein M L 1992 *J. Chem. Phys.* **101** 4177
[31] Rowley A J, Wilson M and Madden P A 1999 *J. Phys.: Condens. Matter* **11** 1903
[32] See, for example, Payne M C, Teter M P, Allan D C, Arias T A and Joannopoulos J D 1992 *Rev. Mod. Phys.* **64** 1045
[33] Perdew J P 1991 *Physica* B **172** 1
[34] Perdew J P and Wang Y 1992 *Phys. Rev.* B **46** 6671

[35] Ashcroft N W and Mermin N D 1976 *Solid State Physics* (Philadelphia, PA: Saunders)
[36] Blount E I 1962 *Solid State Phys.* **13** 305
[37] Marzari N and Vanderbilt D 1997 *Phys. Rev.* B **56** 12847
[38] King-Smith R D and Vanderbilt D 1993 *Phys. Rev.* B **47** 1651
[39] Vanderbilt D and King-Smith R D 1993 *Phys. Rev.* B **48** 4442
[40] Resta R 1994 *Rev. Mod. Phys.* **66** 899
[41] Resta R 2000 *J. Phys.: Condens. Matter* **12** R107
[42] Souza I, Wilkens T and Martin R M 2000 *Phys. Rev.* B **62** 1666
[43] Bernasconi L, Wilson M and Madden P A 2001 *Comput. Mater. Sci.* **22** 94
[44] Bernasconi L, Madden P A and Wilson M 2002 *Phys. Chem. Commun.* **1** U1
[45] Silvestrelli P L, Marzari N, Vanderbilt D and Parrinello M 1998 *Solid State Commun.* **107** 7
[46] Silvestrelli P L 1999 *Phys. Rev.* B **59** 9703
[47] Wilson M and Madden P A 1997 *Mol. Phys.* **90** 75
[48] Pyper N C 1986 *Phil. Trans. R. Soc.* A **320** 107
[49] Fowler P W and Pyper N C 1985 *Proc. R. Soc.* A **398** 377
[50] Liu Y Y, Billone M V, Fischer A K, Tam S W and Clemmer R G 1985 *J. Fus. Tech.* **8** 1970
[51] Farley T W D, Hayes W, Hull S, Hutchings M T and Vrtis M 1991 *J. Phys.: Condens. Matter* **3** 4761
[52] Dovesi R, Roetti C, Freyria-Fava C, Prencipe M and Saunders V R 1991 *Chem. Phys.* **156** 11
[53] Shukla A, Dolg M, Fulde P and Stoll H 1998 *J. Chem. Phys.* **108** 8521
[54] Nosé S 1984 *J. Chem. Phys.* **81** 511
Hoover W G 1985 *Phys. Rev.* A **31** 1695
[55] Kurasawa T, Takahashi T, Noda K, Takeshita H, Nasu S and Watanbe H 1982 *J. Nucl. Mater.* **107** 334
[56] Farley T W D, Hayes W, Hull S, Hutchings M T, Alba M and Vrtis M 1989 *Physica* B **156/157** 99
[57] Osaka T and Shindo I 1984 *Solid State Commun.* **51** 421
[58] Laird B B and Haymet A D J 1992 *Chem. Rev.* **92** 1819
[59] Jesson B J and Madden P A 2000 *J. Chem. Phys.* **113** 5935
[60] Hiernaut J P, Hyland G J and Ronchi C 1993 *Int. J. Thermophys.* **14** 259
Hiernaut J P, Hyland G J and Ronchi C 1993 *Int. J. Thermophys.* **14** 609
[61] Hansen J-P and McDonald I R 1986 *Theory of Simple Liquids* (New York: Academic)
[62] Oishi Y, Kamei Y, Akiyama M and Yanagi T 1979 *J. Nucl. Mater.* **87** 341